Quantification of breast density with dual energy mammography: An experimental feasibility study

Justin L. Ducote and Sabee Molloi[a)]
Department of Radiological Sciences, University of California, Irvine, California 92697

Purpose: Breast density, the percentage of glandular breast tissue, has been shown to be a strong indicator of breast cancer risk. A quantitative method to measure breast density with dual energy mammography was investigated using physical phantoms.

Methods: The dual energy mammography system used a tungsten anode x-ray tube with a 50 μm rhodium beam filter for low energy images and a 300 μm copper beam filter for high energy images. Glandular and adipose equivalent phantoms of uniform thickness were used to calibrate a dual energy basis decomposition algorithm. Four different phantom studies were used to evaluate the technique. The first study consisted of phantoms with thicknesses of 2.5–8.5 cm in 0.5 cm steps with variable densities centered at a mean of 28%. The second study consisted of phantoms at a fixed thickness of 4.0 cm, which ranged in densities from 0% to 100% in increments of 12.5%. The third study consisted of 4.0 cm thick phantoms at densities of 25%, 50% and 75% each imaged at three areal sizes, approximately 62.5, 125, and 250 cm^2, in order to assess the effect of breast size on density measurement. The fourth study consisted of step phantoms designed to more closely mimic the shape of a female breast with maximal thicknesses from 3.0 to 7.0 cm at a fixed density of 50%. All images were corrected for x-ray scatter.

Results: The RMS errors in breast density measurements were 0.44% for the variable thickness phantoms, 0.64% for the variable density phantoms, 2.87% for the phantoms of different areal sizes, and 4.63% for step phantoms designed to closely resemble the shape of a breast.

Conclusions: The results of the phantom studies indicate that dual energy mammography can be used to measure breast density with an RMS error of approximately 5%. © *2010 American Association of Physicists in Medicine*. [DOI: 10.1118/1.3284975]

Key words: mammography, breast density, dual energy, breast imaging, cancer

I. INTRODUCTION

Breast density, the percentage of glandular tissue in a female breast, has been identified as an important risk factor in the development of breast cancer.[1] The current standard of care for breast density evaluation involves visual assessment of mammograms using the four-category breast imaging reporting and data system. This subjective classification scheme is limited by its considerable intrareader and inter-reader variability.[2] Several groups have reported more quantitative approaches[3–5] for measuring breast density. Area-based techniques have included qualitative and semiquantitative classification schemes,[3,6,7] and quantitative estimations from manual or semimanual segmentation of a digital image histogram.[6] Although these quantitative measures provide a more quantitative measure of breast density, one of the limitations is the binary classification of a pixel into either 100% glandular or 100% adipose tissue. Additionally, an important limitation is that an area measurement ignores the physical 3D character of a real breast. Breasts of different thicknesses can potentially all yield the same measurement of area breast density yet correspond to widely varying volumetric breast density values.

Breast cancer risk is most likely more strongly associated with the volume of dense tissue as opposed to the projected area. Volume-based techniques, which overcome some of the limitations of area-based techniques, have included attempts to standardize[8,9] and calibrate[10–12] mammographic image data. However, these techniques require assumptions to be made in order to measure breast density and thickness from a single image. A common assumption of uniform breast thickness is a fundamental limitation of these techniques. The compression paddle thickness is commonly used to estimate breast thickness. Therefore, breast density estimation based on phantom calibration of the system is not valid in the periphery of the breast, since breast thickness is not known in this region. Also, the reported breast thickness from compression paddle may be off by several millimeters in either direction. Furthermore, many clinical mammography systems employ a spring-loaded paddle. The resultant "tilt" of the paddle makes it difficult to assert any region of the mammogram as uniformly thick. It would be advantageous to have a method to measure breast density which does not require the above assumptions.

Breast density can potentially be quantified using dual energy imaging. Dual energy imaging can exploit differences between the effective atomic numbers (Z) of different tissues to provide separate quantitative thickness measurements for each tissue. Previous dual energy mammography techniques have primarily focused on imaging calcium,[13–21] iodine,[22–25]

and neoplastic breast tissue.[26–29] The adipose and glandular tissues have effective atomic numbers of 6.33 and 6.93, respectively.[30] Dual energy mammography can exploit this effective atomic number difference to quantify glandular and adipose tissue thicknesses for breast density measurement. It does not require any assumption for breast density measurement, since glandular and adipose thickness measurements are based on two physical measurements using low and high energy images. Previous attempts at using dual energy x-ray absorptiometry (DXA) for the measurement of breast density[31] were hampered by the beam spectra of the DXA system, which was not optimal for breast density measurement.

We have previously reported a simulation study designed to estimate the required dose to quantify breast density using dual energy mammography.[32] A dual energy mammography system, equipped with a tungsten anode x-ray tube using the standard screening mammogram as the low energy image and an additional exposure at 49 kVp with a 300 μm copper beam filter for the high energy image, was simulated.[32]

The purpose of this study was to carry out a comprehensive phantom study to characterize the accuracy of a dual energy mammography system in quantifying breast density. Breast density measurement errors are presented for four phantom configurations designed to measure a range of phantom thicknesses, densities, sizes, and shapes. Also, the impact of dose on measuring breast density was examined.

II. DUAL ENERGY DECOMPOSITION

It is possible to combine low and high energy images to enhance a particular component in a projection image. However, the presence of nonlinear effects (e.g., beam hardening and x-ray scatter) precludes the use of linear log subtraction for generating accurate quantitative dual energy images. For this reason, nonlinear inverse functions were chosen to recover material thickness values from measured image log signals. A nonlinear eight-term rational function was selected for dual energy calibration.[33] This function was reported to be capable of high fitting accuracy while requiring relatively few terms:

$$t_i = \frac{a_0 + a_1 l + a_2 h + a_3 l^2 + a_4 lh + a_5 h^2}{\sqrt{1 + b_1 l + b_2 h}}. \tag{1}$$

The thickness of each material, t_i, was fit separately to the low and high energy log signals, l and h, respectively, using a nonlinear least-squares minimization algorithm (Levenberg–Marquardt).[34]

Thickness combinations of adipose and glandular phantoms were used to show the ability of dual energy decomposition to distinguish between adipose and glandular tissues. This is illustrated in Fig. 1, where the thicknesses of glandular and adipose equivalent phantoms have been purposely chosen such that there is little difference in signal (i.e., contrast) across the different regions of the low energy image [see Fig. 1(a)]. The low and high [see Fig. 1(b)] energy images were combined to form dual energy adipose [see Fig. 1(c)] and glandular [see Fig. 1(d)] images. It only becomes
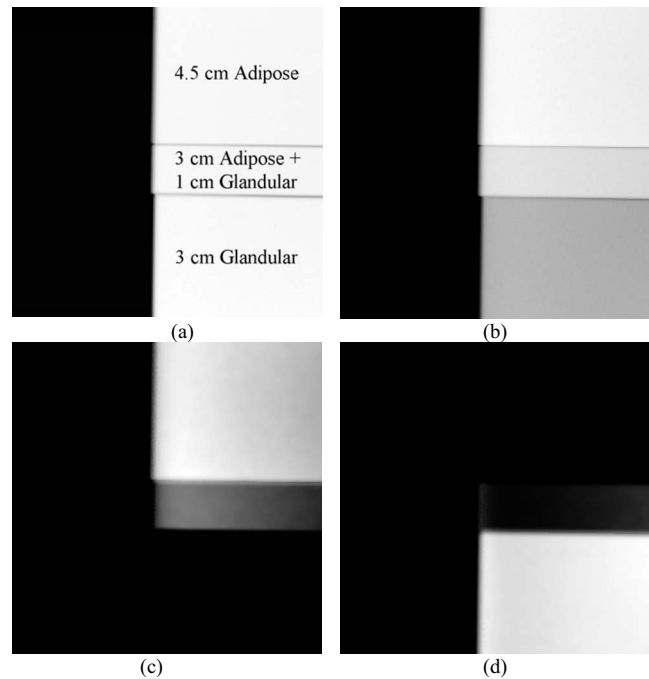

FIG. 1. An illustration of dual energy decomposition. The original (a) low and (b) high energy images along with the dual energy (c) adipose and (d) glandular images are shown. No scatter correction was performed. Actual thicknesses are shown on image (a).

apparent after the dual energy decomposition that the phantom was constructed of two intertwined descending step phantoms. As these images were not corrected for the effects of x-ray scatter, small image gradients and residual edge signals can be seen in the dual energy images.

III. MATERIALS AND METHODS

III.A. Image acquisition and processing

All images in this study were acquired using a full field digital mammography system (Selenia, Hologic, Inc., Bedford MA). This system uses an amorphous selenium (a-Se) direct conversion detector with a Tungsten (W) x-ray tube and maximum beam energy of 49 kVp. The system includes a high-transmission cellular (cross-hatch) grid (4:1 grid ratio, 15 lines/cm). It is configured with two beam filters: A 50 μm rhodium filter and a 300 μm copper filter. The use of a copper filter was employed to increase spectral separation for the high energy beam in a dual energy configuration. The low energy images were acquired at 28 kVp with the rhodium filter at 60 mAs. The high energy images were acquired at 49 kVp with the copper filter at 30 mAs. This technique was referred to as the reference dose level of this study. A second technique was used to assess the impact of dose on measuring breast density for one phantom. For this technique, the mAs values for both the 28 and 49 kVp exposures was set at 4.0, the lowest possible available setting on the system. The calculated mean energies of the low and high energy beams were calculated to be 18.8 and 38.0 keV, respectively. For manual offline gain calibration, a dark field image and an open field image at each energy level was

acquired. The time between each exposure was set to four minutes to minimize the effect of detector ghosting.[35]

All image processing was performed using ImageJ.[36] All low and high energy images were first offset-corrected by subtracting the dark field image, and then normalized by their respective flat field images to remove nonuniformities in the image field. When needed, log signal values were calculated by taking the negative logarithm of each image.

III.B. Scatter correction

X-ray scatter is a major cause of nonlinearity in densitometry measurements using digital mammography. A previously reported technique was used to correct images for x-ray scatter.[37,38] The scatter correction technique is based on image convolution using a spatially variant scatter point spread function, which is energy and thickness dependent. A previously reported technique[39] was used to characterize the scatter kernel in terms of its scattering fraction and radial extent for different phantom thicknesses and beam energies. The algorithm operates on a pixel by pixel basis by grouping pixels of similar thicknesses into a series of mask images that are then individually deconvolved using Fourier image analysis with a distinct kernel for each image.

The previously reported scatter correction technique[37,38] was slightly modified to enhance its performance in a dual energy configuration. The original algorithm estimated pixel thickness from single energy calibrations. This estimation was improved by modifying the algorithm to work in conjunction with the dual energy calibration. An initial dual energy calibration was carried out using low and high energy images before scatter correction. The estimated pixel thicknesses were then used for the scatter correction technique. This ensured that pixel values from the low and high energy images yielded the same thickness estimate. The initial dual energy calibration was only used to estimate pixel thickness for the scatter correction technique.

III.C. Phantom composition and geometry

Glandular and adipose equivalent phantoms of uniform thickness were used for dual energy calibration and phantom studies (CIRS, Norfolk, VA). Each phantom had a uniform thickness with dimensions of 10.0×12.5 cm^2, and was available in discrete thicknesses of 0.5, 1.0, and 2.0 cm. The maximum possible thickness for each phantom material was 8.5 cm. Specific known densities (i.e., percentages of glandular breast tissue), D_k, were achieved by varying the ratio of glandular and adipose material at a particular thickness.

III.D. Calibration

Calibrations were carried out at clinically relevant breast thicknesses and densities. Sixteen points were selected for dual energy calibration. The calibration data set included uniform thickness phantoms of pure glandular tissue up to 8.5 cm in thickness (100% density), pure adipose tissue up to 8.5

TABLE I. Thicknesses and densities of points used for dual energy calibration.

Calibration point no.	Thickness (cm)	Known density
1	0	N/A
2	1	100
3	2	100
4	4	100
5	6	100
6	8.5	100
7	1	0
8	2	0
9	4	0
10	6	0
11	8.5	0
12	3	50
13	4	50
14	5	50
15	7	50
16	8	50

cm in thickness (0% density) and an equal combination of the two (50% density) up to 8.0 cm in thickness. The calibration data set is shown in Table I.

III.E. Phantom studies

Four phantom configurations were investigated. The first study consisted of uniform thickness phantoms with thicknesses of 2.5–8.5 cm in 0.5 cm steps. The range of densities tested varied from 25% to 40% and the mean density of the data set was 28%, which is close to the most recent estimates of clinical breast density.[40] The measurement points used in this phantom study are shown in Table II. The second study consisted of uniform thickness phantoms at a thickness of 4.0 cm, which ranged in density from 0% to 100% in increments of 12.5%. The third study consisted of 4.0 cm uniform

TABLE II. Thicknesses and densities of data set used in the first phantom study.

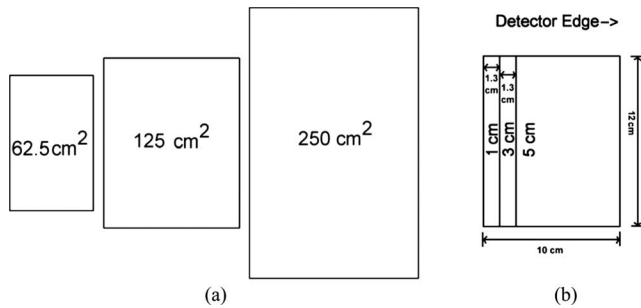| Thickness (cm)	Known density
2.0	25.00
2.5	40.00
3.0	33.33
3.5	28.57
4.0	25.00
4.5	22.22
5.0	30.00
5.5	27.27
6.0	25.00
6.5	30.77
7.0	28.57
7.5	26.67
8.0	25.00
8.5	29.41

FIG. 2. A schematic representation of the 5 cm thick phantom at different areal sizes in the third study (a) and arranged into a step configuration with a maximal thickness of 5 cm in the fourth study (b). The ROIs used were drawn just at the border of the phantoms. The size of the ROIs used in (a) were 66.4, 133.4, and 270.0 cm. The size difference was due to the image magnification of approximately 5%.

TABLE III. The fitting coefficients of each material for the dual energy calibration data. "Pre" and "Post" refer to the fits prior to and after correction for x-ray scatter.

Coefficient Index	Glandular equivalent Pre	Adipose equivalent Pre	Glandular equivalent Post	Adipose equivalent Post
a_0	0.00	0.03	0.08	−0.08
a_1	78.00	−96.78	71.98	−85.91
a_2	−210.10	313.06	−171.19	248.69
a_3	−25.30	18.31	−44.54	39.47
a_4	154.78	−144.69	222.85	−230.42
a_5	−210.60	235.25	−256.89	307.60
b_1	−0.39	−0.28	−0.62	−0.47
b_2	1.19	0.93	1.72	1.38

thickness phantoms at densities of 25%, 50%, and 75%. Each phantom was imaged at three areal sizes of approximately 62.5, 125, and 250 cm^2 in order to assess the effect of breast size on density measurement. The fourth study consisted of step phantoms designed to more closely mimic the shape of a female breast. The majority of the phantom in the fourth study was approximately uniform in thickness followed by a sharp taper to 0 cm at the periphery of the breast distal to the chest wall. The maximal thicknesses were 3.0–7.0 cm in increments of 1.0 cm, and the density was fixed at 50%. A schematic of the 5 cm thick phantom, used in the third and fourth studies, is shown in Fig. 2.

III.F. Dual energy density measurement

After dual energy decomposition, each pair of low and high energy images yielded images of glandular and adipose material thickness. For each image, a region of interest (ROI) was drawn to encompass the phantom. The mean glandular thickness (T_g), and the mean adipose thickness (T_a) was measured. The mean measured density (D_m) was calculated by dividing the mean glandular thickness by the sum of the mean glandular and adipose thicknesses. This value was multiplied by 100 to convert the fractional density to a percentage as follows:

$$D_m = 100 \times \left(\frac{T_g}{T_g + T_a} \right). \tag{2}$$

For the uniform thickness phantoms, the size and location of each ROI was derived by measuring the entire image to determine the location of each phantom's center-of-mass. The mean of each phantom image was then sampled with a small (∼4.50 cm^2) ROI at the center-of-mass and its standard deviation also measured. Next, three standard deviations were subtracted from the mean to calculate a threshold value for pixels that were assumed to be "uniformly thick." A ROI was then drawn encompassing these thresholded pixels. This procedure allowed for an automated technique of ROI selection that was free of operator involvement. For the fourth study, a user-determined threshold, aimed at attempting to select the entire phantom, was used. This process of drawing ROIs was

carried out on the high energy images and this set of ROIs was used on both low and high energy images without modification.

III.F.1. The effect of dose on measuring density

In order to assess the effect of dose on breast density measurement, a 5.0 cm thick phantom of 30% density was imaged at mean glandular doses of 0.85 mGy (reference) and 0.075 mGy (lowest possible mAs setting on the system). Mean glandular dose values were calculated from estimates of the low and high energy spectral distributions[41] in combination with Monte Carlo simulations of the dose per photon as a function of energy.[42,43]

The quantity of interest in this study is the mean density for the whole breast (D). Given the homogenous nature of the phantoms, the standard deviation in density for a single pixel d was measured, and the variability in whole breast density D was inferred by dividing by the square root of the total number of pixels in the image. In order to ensure a faithful measurement of stochastic pixel variance, two independent density images were subtracted from one another to remove any structured noise. The standard deviation was then divided by the square root of two.

III.G. Error analysis

The RMS errors in density estimation were calculated according to the following expression:

$$\text{RMSE} = \frac{1}{\sqrt{n}} \sqrt{\sum_{i=1}^{n} (D_m - D_k)^2}. \tag{3}$$

IV. RESULTS

IV.A. Dual energy calibration

Dual energy calibrations were carried out twice. The initial dual calibration prior to scatter correction was only used for thickness estimation in the scatter correction algorithm. The second dual energy calibration using scatter corrected
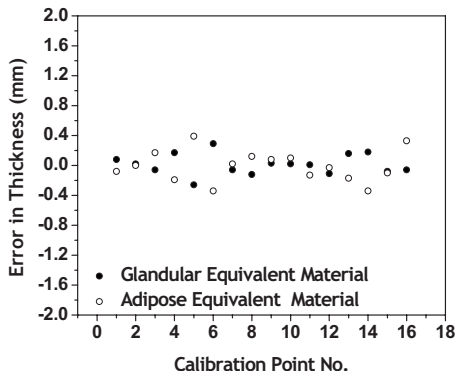
FIG. 3. Fitting errors in thickness at all calibration points for each material. The RMS error in thickness for glandular equivalent material was 0.14 mm and the RMS error in thickness for adipose equivalent material was 0.20 mm.

images was used for breast density measurements. The fitting coefficients for the two calibration data sets are shown in Table III.

The fitting errors in thickness are shown in Fig. 3. The fitting error is the difference between the known thickness and the calculated thickness from Eq. (1), following dual energy calibration. For the 16 point calibration set, the RMS error for glandular equivalent material was 0.18 mm and the RMS error for adipose equivalent material was 0.20 mm. The fitting errors in density at all calibration points are shown in Fig. 4. The RMS error in density was 0.44%. Shown in Fig. 5 are contour plots of the basis decomposition functions for the glandular and adipose thicknesses.

IV.B. The phantom studies

Results after scatter correction for the four phantom studies are tabulated in Tables IV–VII. RMS errors in density were 0.44% for the first study, 0.64% for the second study, 2.87% for the third study, and 4.63% for the fourth study. The results of density measurements for all four studies are shown in Fig. 6. The known (K) and measured (M) densities were related by $M = 1.03\ K - 0.17$. The RMS error for all four phantom studies was 2.25%. The third study had the widest range of areal phantom sizes, and its RMS error in
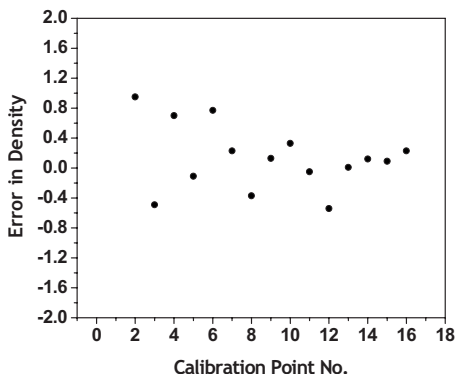

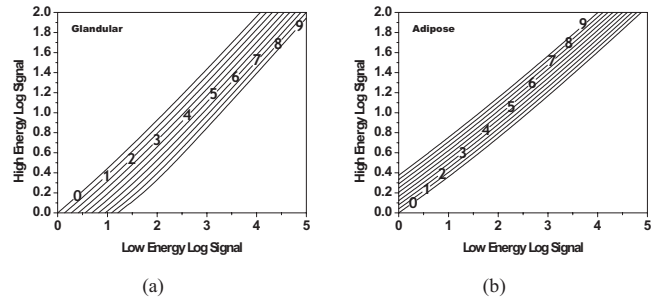FIG. 4. Fitting errors in density at all calibration points. The RMS error was 0.43%.

FIG. 5. Contour plots showing the dependence of glandular (a) and adipose (b) thicknesses on the low and high energy log signals. Lines of isothickness are shown for physical log signal values from 0 to 9 cm.

density alone was 2.87%. The largest single error in density for the study was 6.4% and was part of the fourth study. RMS errors in thickness were 0.17 mm for the first study, 0.34 mm for the second study, and 0.55 mm for the third study. Thickness values, as a whole, were not available for the fourth study as it was a step phantom with no single mean thickness. The RMS errors were instead quantified over the uniform thickness region and measured to be 1.4 mm. The known (K) and measured (M) thicknesses were related by $M = 1.00\ K - 0.41$. The combined RMS error for all four phantom studies was 0.61 mm. Preliminary thickness and density measurements prior to scatter correction were also included for the third study in Table VI. There, the RMS error in density was 5.04% and the RMS error in thickness was 0.77 mm.

Detector signals for the phantom studies were also used to quantify the change in signal before and after correcting for x-ray scatter, and are tabulated in Table VIII for the 50% dense phantom of the third study. The mean scatter fraction for the 125.0 cm^2 phantom was estimated at 15.3% for the high energy beam and 8.2% for the low energy beam.

IV.C. The effect of dose

For a 5 cm thick phantom of 30% density and reference dose of 0.85 mGy, the percent relative standard deviation (%RSD) in whole breast density was measured to be 0.02%. For a dose of 0.075 mGy, the %RSD in whole breast density was measured to be 0.15%, which is approximately seven times greater than the reference dose.

V. DISCUSSION

The RMS error in dual energy calibration thickness estimation was found to be less than 1 mm for glandular and adipose materials. Individual errors in glandular and adipose thicknesses at each point in the calibration appeared to be negatively correlated. The errors in density were seen to be less than 1% for all points. The small errors indicate that the nonlinear function selected for dual energy calibration was well-matched to the acquired data. This demonstrates a clear advantage of using nonlinear decomposition to construct dual energy images, particularly, the ability of the dual energy calibration to *independently* account for the effects of beam hardening[33] for each material. It was observed that

TABLE IV. Errors in density estimation for the first study of uniform thickness phantoms. The RMS error in thickness for the data set was 0.17 mm and 0.44% in density. The values of l and h refer to the negative log signals of the low and high energy images, respectively. Pre and Post refer to the signals prior to and after correction for x-ray scatter.

Thickness (cm)	Measured thickness (cm)	Thickness error (cm)	Known density	Measured density	Density error	l Pre	l Post	h Pre	h Post
2.0	2.00	−0.004	25.00	24.60	−0.40	1.12	1.16	0.41	0.49
2.5	2.49	−0.008	40.00	39.23	−0.77	1.48	1.53	0.53	0.63
3.0	3.00	0.002	33.33	32.94	−0.39	1.72	1.79	0.63	0.75
3.5	3.49	−0.011	28.57	28.77	0.20	1.95	2.03	0.73	0.87
4.0	4.00	−0.002	25.00	24.97	−0.03	2.19	2.27	0.83	0.99
4.5	4.51	0.009	22.22	21.32	−0.91	2.41	2.51	0.93	1.12
5.0	4.99	−0.011	30.00	29.97	−0.03	2.75	2.86	1.05	1.26
5.5	5.50	−0.001	27.27	27.41	0.13	2.99	3.10	1.15	1.39
6.0	6.00	0.000	25.00	24.86	−0.14	3.21	3.33	1.25	1.51
6.5	6.52	0.023	30.77	30.55	−0.22	3.55	3.68	1.38	1.66
7.0	7.03	0.025	28.57	28.75	0.18	3.77	3.92	1.48	1.79
7.5	7.53	0.028	26.67	26.46	−0.20	3.98	4.15	1.58	1.91
8.0	8.04	0.041	25.00	24.76	−0.24	4.21	4.38	1.68	2.04
8.5	8.50	−0.001	29.41	30.26	0.85	4.53	4.72	1.80	2.18

TABLE V. Errors in density estimation for the second study of phantoms at a fixed thickness and variable density. The RMS error in thickness for the data set was 0.34 mm and 0.64% in density. The values of l and h refer to the negative log signals of the low and high energy images, respectively. Pre and Post refer to the signals prior to and after correction for x-ray scatter.

Thickness (cm)	Measured thickness (cm)	Thickness error (cm)	Known density	Measured density	Density error	l Pre	l Post	h Pre	h Post
4.0	3.99	−0.015	0.00	−0.19	−0.19	1.94	2.03	0.77	0.94
4.0	3.99	−0.011	12.50	24.61	−0.39	2.18	2.26	0.83	0.99
4.0	3.96	−0.035	25.00	13.24	0.74	2.06	2.14	0.80	0.96
4.0	3.96	−0.037	37.50	38.02	0.52	2.29	2.38	0.85	1.01
4.0	3.98	−0.018	50.00	50.49	0.49	2.42	2.50	0.88	1.05
4.0	3.97	−0.031	62.50	63.35	0.85	2.53	2.62	0.90	1.07
4.0	3.96	−0.044	75.00	75.93	0.93	2.64	2.72	0.93	1.09
4.0	3.96	−0.042	87.50	87.90	0.40	2.75	2.83	0.95	1.12
4.0	3.95	−0.050	100.00	100.83	0.83	2.86	2.94	0.98	1.14

TABLE VI. Errors in thickness and density estimation for the third study of phantoms at a fixed thickness, variable density, and variable areal size. Prior to scatter correction, the RMS error in thickness for the data set was 0.77 mm and 5.04% in density. After scatter correction, the RMS error in thickness for the data set was 0.55 mm and 2.87% in density. The values of l and h refer to the negative log signals of the low and high energy images, respectively. Pre and Post refer to the signals prior to and after correction for x-ray scatter.

Thickness (cm)	Areal size (cm²)	Measured thickness (cm) Pre	Thickness Error (cm) Pre	Measured thickness (cm) Post	Thickness error (cm) Post	Known density	Measured density Pre	Density error Pre	Measured density Post	Density error Post	l Pre	l Post	h Pre	h Post
4.0	62.45	4.09	0.090	3.92	−0.079	25	18.90	−6.10	28.43	3.43	2.18	2.26	0.84	0.98
4.0	125.0	3.98	−0.017	3.98	−0.019	25	25.02	0.02	25.40	0.40	2.18	2.27	0.83	0.99
4.0	254.877	3.89	−0.105	4.00	−0.002	25	30.32	5.32	24.64	−0.36	2.19	2.27	0.82	0.99
4.0	62.23	4.08	0.077	3.90	−0.099	50	43.87	−6.13	54.85	4.85	2.41	2.50	0.89	1.03
4.0	125.00	4.01	0.006	4.00	0.003	50	49.81	−0.19	50.19	0.19	2.43	2.51	0.88	1.05
4.0	252.94	3.91	−0.091	4.01	0.014	50	56.20	6.20	49.61	−0.39	2.43	2.51	0.88	1.05
4.0	61.81	4.08	0.078	3.90	−0.102	75	68.72	−6.28	81.16	6.16	2.65	2.73	0.94	1.09
4.0	125.00	3.99	−0.014	3.98	−0.018	75	75.32	0.32	75.69	0.69	2.65	2.74	0.93	1.10
4.0	254.78	3.89	−0.113	3.99	−0.011	75	81.90	6.90	74.72	−0.28	2.65	2.73	0.92	1.10

TABLE VII. Errors in density estimation for the fourth study of phantoms at a variable thickness and fixed density. The RMS error in thickness for the data set was 1.4 mm and was 4.63% in density. The values of l and h refer to the negative log signals of the low and high energy images, respectively. Pre and Post refer to the signals prior to and after correction for x-ray scatter.

Maximal step thickness (cm)	Measured thickness (cm)	Thickness error (cm)	Known density	Measured density	Density error	l Pre	l Post	h Pre	h Post
3.0	2.94	−0.061	50.00	52.62	2.62	1.84	1.90	0.65	0.77
4.0	3.89	−0.112	50.00	53.94	3.94	2.41	2.49	0.87	1.03
5.0	4.83	−0.167	50.00	54.56	4.56	2.97	3.07	1.09	1.29
6.0	5.89	−0.114	50.00	54.81	4.81	3.55	3.67	1.32	1.57
7.0	6.80	−0.201	50.00	56.40	6.40	4.09	4.23	1.54	1.83

beam hardening caused a difference in attenuation between the 1.0 and 8.5 cm thickness phantoms of 7.5% for adipose tissue, whereas the difference was 12% for glandular tissue. It is also important to point out that the dual energy system seemed stable over time and did not require any recalibration. The data for this study was collected over a time frame of approximately six months, and the results showed no significant indications of system drift or degraded accuracy over this period of time.

In order to minimize ghosting and lag, the low and high energy images in this study were acquired approximately four minutes apart. For clinical implementation of dual energy mammography, newer detectors, such as the ones being considered for tomosynthesis will be used. These detectors have been reported to have markedly lower levels of ghosting and lag.[35] With acquisition rates of up to 4 frames/s, the required time for dual energy exposure could fall to 0.5 s. This short time interval will minimize the potential misregistration artifacts between low and high energy images.

Also, the low energy data for this study were acquired at a single energy of 28 kVp. In practice, several low energies may be encountered. One limitation of this technique in its current form is that it requires an independent calibration data set of approximately 16 images for each expected low energy technique. It is possible to reduce the required workload by constructing a multipoint phantom designed for dual energy calibration. A similar technique has previously been used for calcium imaging.[44] This was not done in this study, as only one phantom set was available for testing. The number of calibration images for each kVp would be reduced from approximately 16 to one. This seems to be a reasonable

approach to calibration in a clinical environment and the results are not expected to change, regardless of the kVp of the low energy beam.

The results from the first two studies, using uniform phantoms, provided a wide range of thicknesses and densities to test and validate the dual energy calibration technique. While the data in the studies one and two shared the same areal size as the data used for calibration, there was only one overlapping thickness and density point. This indicates that the dual energy calibration technique can be used for decomposition of adipose and glandular tissue.

X-ray scatter is the predominant source of error in breast density measurement using dual energy mammography. Furthermore, scatter intensity is highly dependent on object thickness. In order to estimate object thickness, dual energy decomposition was performed using the low and high energy images prior to scatter correction. The object thickness estimate was then used in the scatter correction technique[37,38] for accurate scatter estimation. The final dual energy decomposition and breast density measurements were done using scatter corrected images. This approach can be considered an iterative method as the results from the first dual energy calibration were used to estimate object thickness. The scatter corrected images were then recalibrated and subsequent thickness and density estimates were superior to the original measurements as seen from the data in Table VI. This also suggests that additional iterations might provide further benefit. However, our results here indicate that a first order

TABLE VIII. Relative detector signals in the third study for pre and post scatter correction.

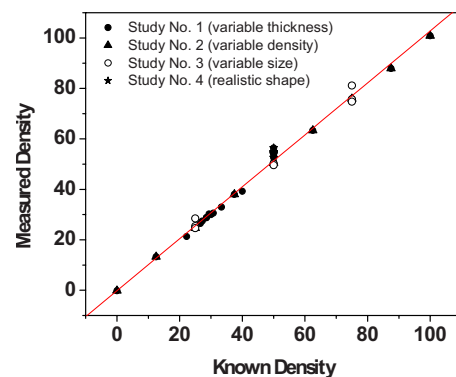| kVp	Areal size (cm^2)	Rel. detector signal— Precorrection (arbitrary units)	Rel. detector signal— Postcorrection (arbitrary units)
	62.5	101.7	93.5
28	125.0	100.0	91.8
	250.0	99.7	91.7
	62.5	99.7	86.2
49	125.0	100.0	84.7
	250.0	100.9	84.5

FIG. 6. The results of density measurements for all four phantom studies. The known (k) and measured (m) densities were related by $M = 1.03$ K−0.17. The RMS error for all four phantom studies was 2.25%.

thickness estimate using a dual energy decomposition is adequate for the scatter correction necessary for accurate breast density measurement.

In the results, it was seen that the scatter corrected detector signal is slightly higher for the smaller field size (see Table VIII). This is also the case for low energy image prior to scatter correction where the scatter fraction is relatively small as compared to the high energy image. The difference in detector signal is expected to be due to the difference in beam attenuation for different field sizes. The smallest phantom image is generated by placing the full size phantom on the edge of the detector in order to reduce the exposed area of the phantom by approximately half. The x-ray tube is aligned such that the location of the central ray is close to the edge of the detector. The other two phantoms occupy more pixels which are distal to the edge of the detector and the path length is, on average, longer due to the fact that the angle of incident x-ray photons is no longer perpendicular with the surface of the detector. This increases the effective attenuation for the larger phantoms.

The focus of this study was to test the experimental feasibility of dual energy mammography to measure breast density in the presence of beam hardening, possible detector nonuniformities, and x-ray scatter. In regards to the required radiation dose, our previous study predicted dose levels of approximately $10-20$ μGy to measure the %RSD within $1/3$%.[32] In this study, the lowest achievable dose level on the mammography system was approximately 75 μGy, and the %RSD was calculated to be 0.15%. Given that this dose is approximately five times greater than what was predicted in the simulation study, it generally agrees with the quantum statistics that the measured %RSD was 50% less than the predicted $1/3$%. This suggests that our current experimental results are in general agreement with the predictions made by the simulation model.

In order for dual energy mammography to work in conjunction with digital screening mammography, and be suitable for clinical implementation, a few technical details need to be considered. (1) The separation in mean energies between the two beams should be maximized. (2) The detector lag between low and high energy images should be minimized. (3) The time between exposures should be small to minimize patient discomfort and motion misregistration artifacts. Newer generation digital mammography detectors can potentially address the second and third considerations. The high energy beam filter used in this technique adequately satisfies the first consideration, and could potentially be incorporated into a clinical mammography system without much difficulty.

It is also important to determine the extent in which glandular and adipose equivalent phantoms accurately represent biological tissue. An earlier study that used DXA to measure breast density[31] reported peak low and high beam energies of 70 and 100 keV. Their follow-up report discussed the difficulties when trying to accurately measure breast density, which were found to arise due to the imperfect agreement of x-ray attenuation between phantom and biological tissues at the high beam energies used in the DXA system.[31] In this study, the mean energies of the two beams were 18.8 and 38.0 keV. These energies are closer to and within the recommended 15–40 keV energy range specified by the manufacturer of the mammography phantom reference materials (CIRS, Norfolk, VA) for maximum attenuation agreement. The impact of the difference between phantoms and biological tissue on breast density measurement requires further investigation.

In summary, the results of the phantom studies indicate that dual energy mammography can be used to measure breast density with an RMS error of approximately 5%. Dual energy mammography can potentially be implemented with minimal changes to the standard mammography exam.

ACKNOWLEDGMENTS

[a]Author to whom correspondence should be addressed. Electronic mail: symolloi@uci.edu

[1]N. F. Boyd, H. Guo, L. J. Martin, L. Sun, J. Stone, E. Fishell, R. A. Jong, G. Hislop, A. Chiarelli, S. Minkin, and M. J. Yaffe, "Mammographic density and the risk and detection of breast cancer," N. Engl. J. Med. **356**(3), 227–236 (2007).

[2]S. Ciatto, N. Houssami, A. Apruzzese, E. Bassetti, B. Brancato, F. Carozzi, S. Catarzi, M. P. Lamberini, G. Marcelli, R. Pellizzoni, B. Pesce, G. Risso, F. Russo, and A. Scorsolini, "Categorizing breast mammographic density: Intra- and interobserver reproducibility of BI-RADS density categories," Breast J. **14**(3), 269–275 (2005).

[3]J. N. Wolfe, "Breast patterns as an index of risk for developing breast cancer," AJR, Am. J. Roentgenol. **126**(6), 1130–1137 (1976).

[4]E. A. Sickles, "Wolfe mammographic parenchymal patterns and breast cancer risk," AJR, Am. J. Roentgenol. **188**(2), 301–303 (2007).

[5]L. E. Myers, R. McLelland, C. X. Stricker, S. A. Feig, J. E. Martin, M. Moskowitz, and M. E. Nielsen, Jr., "Reproducibility of mammographic classifications," AJR, Am. J. Roentgenol. **141**(3), 445–450 (1983).

[6]J. W. Byng, N. F. Boyd, E. Fishell, R. A. Jong, and M. J. Yaffe, "The quantitative-analysis of mammographic densities," Phys. Med. Biol. **39**(10), 1629–1638 (1994).

[7]American College of Radiology, *Breast Imaging Reporting and Data System (BI-RADS) Atlas-Mammography*, 4th ed. (The American College of Radiology, Reston, 2003).

[8]R. Highnam, M. Brady, and B. Shepstone, "A representation for mammographic image processing," Med. Image Anal. **1**(1), 1–18 (1996).

[9]R. Highnam, X. Pan, R. Warren, M. Jeffreys, G. Davey Smith, and M. Brady, "Breast composition measurements using retrospective standard mammogram form (SMF)," Phys. Med. Biol. **51**(11), 2695–2713 (2006).

[10]J. Kaufhold, J. A. Thomas, J. W. Eberhard, C. E. Galbo, and D. E. Trotter, "A calibration approach to glandular tissue composition estimation in digital mammography," Med. Phys. **29**(8), 1867–1880 (2002).

[11]O. Pawluczyk, B. J. Augustine, M. J. Yaffe, D. Rico, J. Yang, G. E. Mawdsley, and N. F. Boyd, "A volumetric method for estimation of breast density on digitized screen-film mammograms," Med. Phys. **30**(3), 352–364 (2003).

[12]J. A. Shepherd, L. Herve, J. Landau, B. Fan, K. Kerlikowske, and S. R. Cummings, "Novel use of single X-ray absorptiometry for measuring breast density," Technol. Cancer Res. Treat. **4**(2), 173–182 (2005).

[13]P. C. Johns and M. J. Yaffe, "Theoretical optimization of dual-energy x-ray imaging with application to mammography," Med. Phys. **12**(3), 289–296 (1985).

[14]P. C. Johns, D. J. Drost, M. J. Yaffe, and A. Fenster, "Dual-energy mammography: Initial experimental results," Med. Phys. **12**(3), 297–304 (1985).

[15]S. C. Kappadath and C. C. Shaw, "Quantitative evaluation of dual-energy digital mammography for calcification imaging," Phys. Med. Biol. **49**(12), 2563–2576 (2004).

[16]K. Bliznakova, Z. Kolitsi, and N. Pallikarakis, "Dual-energy mammography: Simulation studies," Phys. Med. Biol. **51**(18), 4497–4515 (2006).

[17]X. Mou and X. Chen, in *Error analysis of calibration materials on dual-energy mammography*, Proceedings of the 10th International Conference on Medical Image Computing and Computer Assisted (Brisbane, Australia), Lect. Notes Comput. Sci. **4792**, 596–603 (2007).

[18]M. E. Brandan and R. V. Ramirez, "Evaluation of dual-energy subtraction of digital mammography images under conditions found in a commercial unit," Phys. Med. Biol. **51**(9), 2307–2320 (2006).

[19]D. P. Chakraborty and G. T. Barnes, "An energy sensitive cassette for dual-energy mammography," Med. Phys. **16**(1), 7–13 (1989).

[20]J. M. Boone, G. S. Shaber, and M. Tecotzky, "Dual-energy mammography: a detector analysis," Med. Phys. **17**(4), 665–675 (1990).

[21]D. S. Brettle and A. R. Cowen, "Dual-energy digital mammography utilizing stimulated phosphor computed radiography," Phys. Med. Biol. **39**(11), 1989–2004 (1994).

[22]J. M. Lewin, P. K. Isaacs, V. Vance, and F. J. Larke, "Dual-energy contrast-enhanced digital subtraction mammography: feasibility," Radiology **229**(1), 261–268 (2003).

[23]H. Bornefalk, J. M. Lewin, M. Danielsson, and M. Lundqvist, "Single-shot dual-energy subtraction mammography with electronic spectrum splitting: Feasibility," Eur. J. Radiol. **60**(2), 275–278 (2006).

[24]M. Saito, "Dual-energy approach to contrast-enhanced mammography using the balanced filter method: Spectral optimization and preliminary phantom measurement," Med. Phys. **34**(11), 4236–4246 (2007).

[25]P. Baldelli, A. Bravin, C. Di Maggio, G. Gennaro, A. Sarnelli, A. Taibi, and M. Gambaccini, "Evaluation of the minimum iodine concentration for contrast-enhanced subtraction mammography," Phys. Med. Biol. **51**(17), 4233–4251 (2006).

[26]A. Taibi, S. Fabbri, P. Baldelli, C. di Maggio, G. Gennaro, M. Marziani, A. Tuffanelli, and M. Gambaccini, "Dual-energy imaging in full-field digital mammography: a phantom study," Phys. Med. Biol. **48**(13), 1945–1956 (2003).

[27]T. Asaga, C. Masuzawa, A. Yoshida, and H. Matsuura, "Dual-energy subtraction mammography," J. Digit Imaging **8**(1), 70–73 (1995).

[28]T. Asaga, S. Chiyasu, S. Mastuda, H. Mastuura, H. Kato, M. Ishida, and T. Komaki, "Breast imaging: Dual-energy projection radiography with digital radiography," Radiology **164**(3), 869–870 (1987).

[29]M. Marziani, A. Taibi, A. Tuffanelli, and M. Gambaccini, "Dual-energy tissue cancellation in mammography with quasi-monochromatic x-rays," Phys. Med. Biol. **47**(2), 305–313 (2002).

[30]T. Fujisaki, M. Kimura, H. Saitoh, S. Abe, and T. Hiraoka, "Production design and evaluation of a novel breast phantom with various breast glandular fractions," Radiat. Med. **24**(10), 647–652 (2006).

[31]J. A. Shepherd, L. Herve, J. Landau, B. Fan, K. Kerlikowske, and S. R. Cummings, "Clinical comparison of a novel breast DXA technique to mammographic density," Med. Phys. **33**(5), 1490–1498 (2006).

[32]J. L. Ducote and S. Molloi, "Quantification of breast density with dual energy mammography: A simulation study," Med. Phys. **35**(12), 5411–5418 (2008).

[33]H. N. Cardinal and A. Fenster, "An Accurate Method for Direct Dual-Energy Calibration and Decomposition," Med. Phys. **17**, 327–341 (1990).

[34]K. Levenberg, "A method for the solution of certain non-linear problems in least squares," Q. Appl. Math. **2**, 164–168 (1944).

[35]A. K. Bloomquist, M. J. Yaffe, G. E. Mawdsley, D. M. Hunter, and D. J. Beideck, "Lag and ghosting in a clinical flat-panel selenium digital mammography system," Med. Phys. **33**(8), 2998–3005 (2006).

[36]M. D. Abramoff, P. J. Magelhaes, and S. J. Ram, "Image processing with ImageJ," Biophotonics Int. **11**(7), 36–42 (2004).

[37]J. L. Ducote and S. Molloi, "Scatter correction in digital mammography based on image deconvolution," Phys. Med. Biol. (in press).

[38]J. L. Ducote and S. Molloi, "SU-FF-I-137: Scatter correction in quantitative dual energy mammography," Med. Phys. **36**(6), 2466 (2009).

[39]J. A. Seibert, O. Nalcioglu, and W. W. Roeck, "Characterization of the veiling glare PSF in x-ray image intensified fluoroscopy," Med. Phys. **11**(2), 172–179 (1984).

[40]T. R. Nelson, L. I. Cervino, J. M. Boone, and K. K. Lindfors, "Classification of breast computed tomography data," Med. Phys. **35**(3), 1078–1086 (2008).

[41]R. Nowotny and A. Höfer, "Ein Programm füer die Berechnung von diagnostischen Röntgenspektren," Fortschr Röntgenstr **142**, 685–689 (1985).

[42]J. M. Boone, "Glandular breast dose for monoenergetic and high-energy x-ray beams: Monte Carlo assessment," Radiology **213**(1), 23–37 (1999).

[43]J. M. Boone, "Normalized glandular dose (DgN) coefficients for arbitrary x-ray spectra in mammography: Computer-fit values of Monte Carlo derived data," Med. Phys. **29**(5), 869–875 (2002).

[44]C. M. Fivez, P. Wambacq, P. Suetens, and E. Schoeters, "Calibration phantom for dual-energy basis material absorption measurements," Proceedings of SPIE–the International Society for Optical Engineering **2708**, 599–608 (1996).